Chin. Phys. Lett. **39**, 047301 (2022) **Express Letter**

Two-Dimensional Electron Gas with High Mobility Forming at $BaO/SrTiO_3$ Interface

Cheng Cao(曹程)[1,3†], Shengru Chen(陈盛如)[1,2†], Jun Deng(邓俊)[1], Gang Li(李岗)[1,4], Qinghua Zhang(张庆华)[1], Lin Gu(谷林)[1], Tian-Ping Ying(应天平)[1,4], Er-Jia Guo(郭尔佳)[1,2,4*], Jian-Gang Guo(郭建刚)[1,4*], and Xiaolong Chen(陈小龙)[1,2,4*]

[1]*Beijing National Laboratory for Condensed Matter Physics, Institute of Physics, Chinese Academy of Sciences, Beijing 100190, China*
[2]*School of Physical Sciences, University of Chinese Academy of Sciences, Beijing 101408, China*
[3]*College of Materials Science and Opto-Electronic Technology, University of Chinese Academy of Sciences, Beijing 100049, China*
[4]*Songshan Lake Materials Laboratory, Dongguan 523808, China*

(Received 26 January 2022; accepted 22 February 2022; published online 3 March 2022)

Two-dimensional electron gas (2DEG) with high electron mobility is highly desired to study the emergent properties and to enhance future device performance. Here we report the formation of 2DEG with high mobility at the interface between rock-salt BaO and perovskite $SrTiO_3$. The interface consists of the ionically compensated $BaO_{1-\delta}$ layer and the electronically compensated TiO_2 layer, which is demonstrated as a perfect interface without lattice mismatch. The so-formed interface features metallic conductivity with ultralow square resistance of $7.3 \times 10^{-4}\,\Omega/\square$ at 2 K and high residual resistance ratios $R_{300\,\mathrm{K}}/R_{2\,\mathrm{K}}$ up to 4200. The electron mobility reaches $69000\,\mathrm{cm^2{\cdot}V^{-1}{\cdot}s^{-1}}$ at 2 K, leading to Shubnikov–de Haas oscillations of resistance. Density functional theory calculations reveal that the effective charge transfers from BaO to the Ti $3d_{xy}$ orbital occur at the interface, leading to the conducting TiO_2 layer. Our work unravels that BaO can adapt itself by removing oxygen to minimize the lattice mismatch and to provide substantial carriers to $SrTiO_3$, which is the key to forming 2DEGs with high mobility at the interfaces.

DOI: 10.1088/0256-307X/39/4/047301

Two-dimensional electron gas (2DEG) confined at the interface between two insulators exhibits exotic properties such as high carrier mobility (μ),[1] interfacial magnetism,[2–4] and superconductivity.[5–9] Extensive effort, including combining versatile materials,[10,11] optimizing polarization of termination,[12,13] tuning lattice mismatch,[14,15] and controlling oxygen vacancies,[16] has been spent to enhance μ and to understand the origin of emergent phenomena. In the most intensively studied $LaAlO_3$ (LAO)/$SrTiO_3$ (STO) interfaces, the polar planes in LAO and non-polar planes in STO match together, resulting in a large compressive strain of 2.97%.[1] Meanwhile, the LAO/STO interface exhibits an unexpected μ of 1000–10000 $\mathrm{cm^2{\cdot}V^{-1}{\cdot}s^{-1}}$ at 2 K.[17–19] It is generally believed that the polar discontinuity at the interface leads to the electronic reconstruction between the electron charged $(LaO)^+$ layer and neutral $(TiO_2)^0$ layer.[20] Once the internal electric potential exceeds the bandgap E_g of STO, it will drive the electrons from the LAO valence band into the STO conduction band. However, the defects and lattice distortion at the interfaces limit the charge transfer and mobility. Building a high-quality interface with minimal misfit is important for improving the μ in 2DEGs. Huang *et al.* replaced the LAO layer with a more lattice-compatible $(La_{0.3}Sr_{0.7})(Al_{0.65}Ta_{0.35})O_3$ layer and reduced the lattice mismatch to be less than 1%, leading to an enhanced μ of $35000\,\mathrm{cm^2{\cdot}V^{-1}{\cdot}s^{-1}}$ at 2 K.[14] Similarly, a record high μ up to $140000\,\mathrm{cm^2{\cdot}V^{-1}{\cdot}s^{-1}}$ was achieved at the interface of spinel-type γ-Al_2O_3 and STO, in which a small lattice mismatch of 1.2% manifests the well-defined interface.[21]

As we know, the $SrTiO_3$ can be viewed as a stack of (SrO) and (TiO_2) layers, where the upmost surface plane generally terminates with a (TiO_2) layer. The simplest and perfect interface is to epitaxially grow binary alkaline-earth-metal oxides AO film on the (TiO_2) layer.[22–26] The AO (A = Ca, Sr, and Ba) possesses the rock-salt structure with lattice parameters between 4.2 and 5.6 Å. Among them, the most compatible phase is BaO and STO because the lattice mismatch is as small as −0.3% between 5.539 Å[24] and $\sqrt{2}a_{\mathrm{STO}}$ (5.523 Å).[1] Notably, BaO shows unique self-adaptability in layered compound $YBa_2Cu_3O_{7-\delta}$ (YBCO),[27–29] in which the linear O–Ba–O bonds can be bent to match the (CuO_2) square lattice and

†These authors contributed equally to this work.
*Corresponding authors. Email: ejguo@iphy.ac.cn; jgguo@iphy.ac.cn; chenx29@iphy.ac.cn
© 2022 Chinese Physical Society and IOP Publishing Ltd

to stabilize the crystal structure.[30] Meanwhile, at the interface of YBCO film and STO, the most stable stacking sequence is $\cdots$SrO–TiO_2–BaO$\cdots$ type.[31] It is suggested that achieving a high-quality interface through growing BaO film on STO is highly feasible and of interest.

In this Letter, we report the epitaxial growth and perfect interface between BaO thin films and STO substrates. The μ at the BaO/STO reaches 69000 $\mathrm{cm^2{\cdot}V^{-1}{\cdot}s^{-1}}$ and 121 $\mathrm{cm^2{\cdot}V^{-1}{\cdot}s^{-1}}$ at 2 K and 300 K, respectively. The itinerate carriers located at the BaO/STO interface are responsible for the exotic transport behaviors, confirmed by our theoretical calculations.

Experimental—Sample Preparation. High-quality BaO thin films were epitaxially grown on [001]-oriented STO substrates by pulses laser deposition. The STO substrates were pretreated by buffered HF and annealed at a high temperature of 1100 ℃ for 1.5 h to ensure TiO_2-terminated surfaces. Before deposition, the base pressure was initially evacuated to 10^{-8} Torr. A 20-nm-thick BaO layer was firstly deposited in vacuum at a substrate temperature of 650–750 ℃ using a polycrystalline BaO_2 pellet. The as-grown BaO film was *in situ* annealed in vacuum at the growth temperature for 1 h. The annealing process was essential for crystallizing the BaO film. After annealing, a 10-nm-thick STO was deposited as a capping layer to prevent the BaO films from reacting with H_2O and CO_2 in air.

Structural Characterization. The lattice parameters and crystalline quality of BaO films were determined by x-ray diffraction (XRD) and ϕ-scans. XRD measurements were conducted on a high-resolution four-circle diffractometer with Cu K_α radiation (Bruker D8 Discovery). The ϕ-scans were taken around the 113 reflections of the BaO films and STO. Scanning transmission electron microscopy (STEM) specimens were prepared using the standard focused ion beam lift-out process. High-angle annular dark-field (HAADF) and annular-bright-field (ABF) imaging were performed in the STEM mode using a JEM ARM 200CF microscope in Institute of Physics, Chinese Academy of Sciences.

Transport Measurement. Transport properties of the BaO films were measured using a four-probe van der Pauw method. The electrodes were ultrasonically wire-bonded Al wires and placed at the corners of the square samples. The BaO films can be contacted directly using wire-bonding through the STO capping layer. Temperature-dependent resistance and Hall measurements were conducted on a physical property measurement system in the temperature range from 2 K to 300 K. The transport measurements with temperatures below 2 K were performed in a sorption pumped ^{3}He cryostat with standard lock-in technique. The magnetic field of the ^{3}He cryostat was applied up to 18 T. During all the transport measurements, the applied currents were 200 μA (for ac current, the frequency was 30.99 Hz) to avoid the heating effects.

Theoretical Calculation. The first-principles calculations were carried out with the density functional theory implemented in the Vienna *ab initio* simulation package (VASP).[32] We adopted the generalized gradient approximation in the Perdew–Burke–Ernzerhof form[33] for the exchange-correlation potentials. The projector augmented-wave[34] pseudopotentials were used with a plane wave energy 500 eV. A Monkhorst–Pack[35] Brillouin zone sampling grid with a resolution $0.02 \times 2\pi$ $\mathrm{Å^{-1}}$ was applied. The atomic positions and lattice parameters were relaxed until all the strain forces on each atom were less than 10^{-2} eV/Å, the results are close to their bulk values. For the BaO/STO interface model without oxygen vacancies, the atomic positions were relaxed until all the forces on the atoms near the interface were less than 5×10^{-2} eV/Å and a $9 \times 9 \times 1$ k-mesh was used in sampling the Brillouin. For the BaO/STO interface model with oxygen vacancies ($2 \times 2 \times 1$ superlattice of BaO/STO), only the Γ point was used in the Brillouin sampling.

Results and Discussions. The BaO films were epitaxially grown on the STO substrates by pulsed laser deposition. After the growth, a 10-nm-thick STO layer was capped on top to protect BaO films. XRD measurements were performed to check the crystallinity of the BaO films. Figure 1(b) shows a typical XRD θ–2θ curve of a BaO thin film grown on an STO substrate. Only 00l reflections from the BaO and STO are observed, indicating that the film is epitaxially grown on the substrate. The out-of-plane lattice constant of the BaO films is 5.528 Å, so the calculated lattice mismatch is 0.23%. Meanwhile, the rocking curve of the BaO 002 peak has a full width at half maximum (FWHM) of 0.338° [inset of Fig. 1(b)]. We think that the interface between BaO/STO can be viewed as a perfect interface under such uncertainties. Figure 1(c) shows the in-plane ϕ-scans of the BaO film and the STO substrate around the (113) plane. Four sharp and discrete peaks are equally separated by 90°, revealing that both film and substrate have a fourfold rotational symmetry, in agreement with their cubic structures. Note that the BaO 113 peak shifts by 45° compared to that of STO, providing solid evidence for rotating BaO in-plane toward the diagonal of the STO, i.e., BaO [110]//STO [100] [Fig. 1(a)], with minimized misfit. Furthermore, we performed the cross-sectional HAADF imaging on the BaO/STO using STEM. Since the BaO is extremely sensitive to the moisture in air during the specimen preparation, only a few unit cells of BaO at the interface are captured. In the HAADF-STEM images, the intensity scales with the value of $Z^{1.7}$, where Z is the atomic

number of elements. The brighter spots correspond to the heavier elements. In Fig. 1(d), the brighter spots represent the Ba atoms, and the weaker spots are the Sr atoms, followed by the Ti atoms. The STEM measurements reveal that a high degree of coherent structure maintains at the interface between BaO and STO. Figure 1(e) shows the ABF-STEM image at the BaO/STO interface. The high-magnified ABF image helps to identify the positions of the O atoms and to further confirm the orientation and epitaxial growth of BaO thin films.

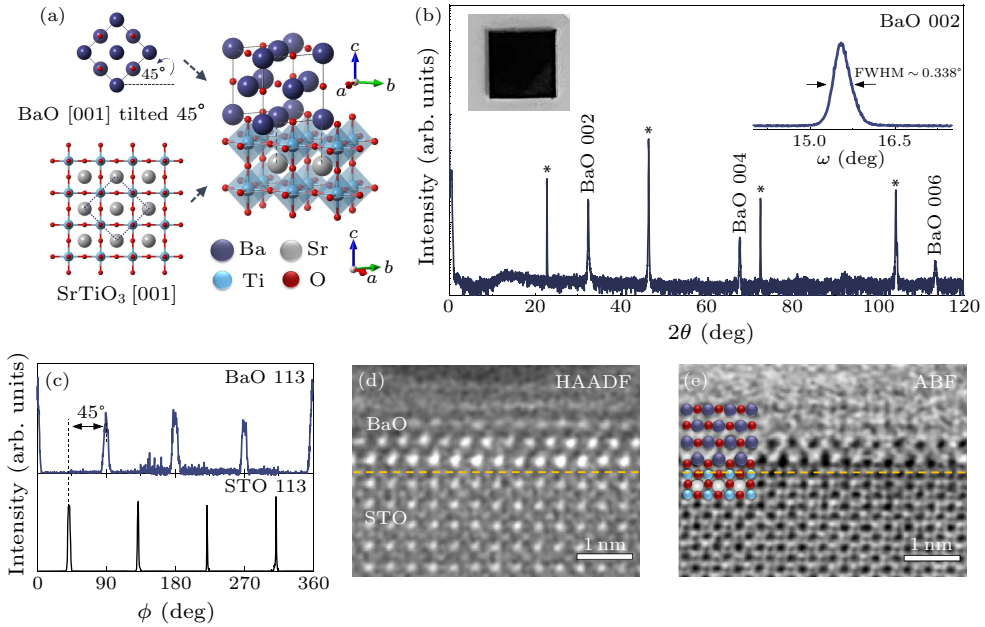

Fig. 1. Crystal structure and epitaxial growth of BaO film. (a) Schematic structure of BaO films on the STO substrates. The unit cell of BaO rotates in-plane by 45° with respect to STO. (b) XRD θ–2θ scan of BaO/STO. The left inset is an optical image of the BaO/STO sample. Right inset shows the rocking curve of the 002 peak with FWHM of 0.338°. (c) Results of ϕ-scans around the 113 reflections of a BaO film (top) and an STO substrate (bottom). (d) Cross-sectional HAADF image and (e) ABF image at the BaO/STO interface taken in the STEM mode. Inset shows the atomic arrangements.

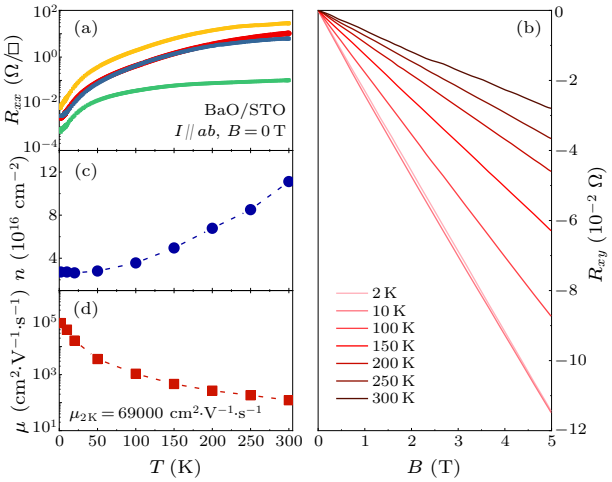

Fig. 2. Transport properties of the BaO/STO. (a) Temperature-dependent sheet resistance R_{xx} of four BaO/STO samples with RRR up to 4200. (b) Magnetic field B dependence of Hall resistance R_{xy} of BaO/STO at various temperatures. (c) Carrier density n and (d) carrier mobility μ, derived from Hall measurements using a single band model versus temperature.

To investigate the transport behavior of BaO films, we firstly measured the temperature-dependent sheet resistance (R_{xx}) of the BaO films under zero magnetic field. In Fig. 2(a), the BaO films exhibit metallic behavior down to 2 K with ultralow R_{xx} of $7.3 \times 10^{-4}\,\Omega/\square$, which is comparable to those of bulk Cu[36] and Sr_2CrMoO_6 (52 nΩ·cm at 2 K).[37] The residue resistance rations [RRR = $R_{xx}(300\,\mathrm{K})/R_{xx}(2\,\mathrm{K})$] are 140–4200. An ultrahigh RRR is a rare case, indicating that the BaO/STO possesses a high-crystalline quality. To exclude the effect of oxygen vacancies on the transport results, we compared the R_{xx}–T curves of the BaO films deposited at a higher growth temperature of 750 ℃. Typically, the higher growth temperature will lead to the increasing oxygen vacancies in both films and substrates. However, we find that the BaO films transit from a metal to a narrow band-gap semiconductor, as shown in Fig. S1 in the Supplementary Material. These results strongly indicate that the observed metallicity does not come solely from oxygen vacancies in STO[38–40] and we will discuss it later.

Having established the transport behavior of BaO films, we further conducted the Hall measurements to understand its electronic characteristics. For the magnetic fields (B) below 5 T, the Hall resistance (R_{xy}) exhibits the linear behavior at all temperatures, as shown in Fig. 2(b). The carrier density n and car-

rier mobility μ are extracted by fitting the R_{xy}–B curves using a single-band model. Figures 2(c) and 2(d) show the n and μ, respectively, versus temperature. With decreasing temperature from 300 to 2 K, n reduces from 1.1×10^{17} cm^{-2} to 2.7×10^{16} cm^{-2}. Note that n of the BaO film is at least an order of magnitude higher than those of other oxide films grown on STO substrates.[21,41] The calculated μ at 300 K is 121 cm^2·V^{-1}·s^{-1}, which is higher than the typical μ (2–12 cm^2·V^{-1}·s^{-1}) in most STO-based 2DEGs.[1,21] At 2 K, the μ reaches up to 69000 cm^2·V^{-1}·s^{-1}. The observed ultrahigh μ in the BaO films is comparable to those reported in bulk Sr_2CrMO_6 (M = Mo, W),[37,42] graphene embedded in metals,[43] and Ca_2N.[44] In addition, the magnetoresistance (MR) linearly increases against B, reaching more than 350% at ±5 T and 2 K. The linear magnetoresistance may be due to the long electron mean free path and high mobility.[45] With increasing temperature, the value of MR decreases dramatically as shown in Fig. S2 in the Supplementary Material.

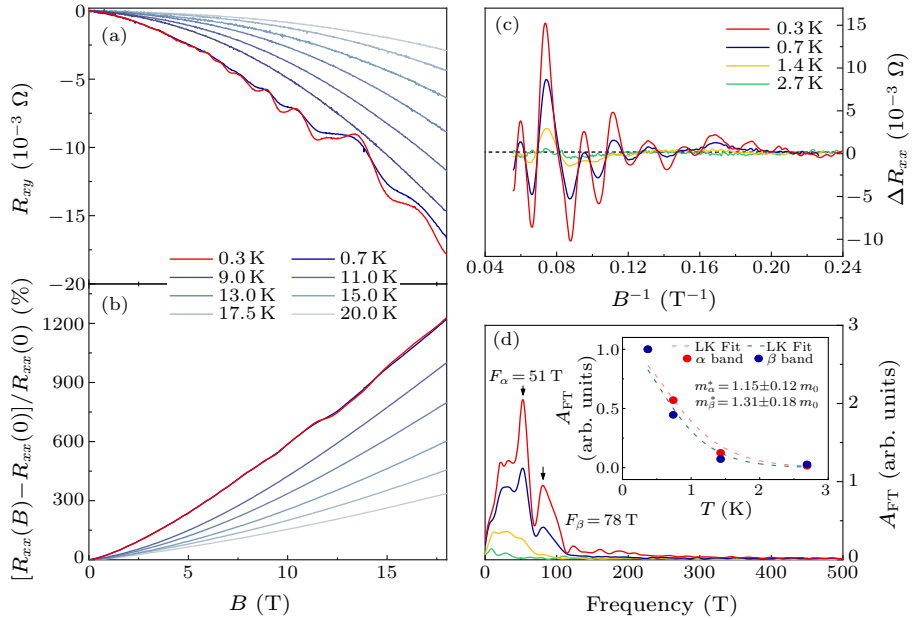

Fig. 3. Observation of quantum oscillation in the BaO/STO. (a) Hall resistance R_{xy} as a function of B at various temperatures. (b) B-dependent magnetoresistance $[R_{xx}(B) - R_{xx}(0)]/R_{xx}(0)$ at different temperatures, where $R_{xx}(B)$ and $R_{xx}(0)$ represent the resistance taken at the magnetic fields of B and zero field, respectively. (c) Shubnikov–de Haas (SdH) oscillations at various temperatures. (d) Fourier transformation (FT) of the ΔR_{xx}–B^{-1} curves in (c), which exhibits oscillatory components with $F_\alpha = 51$ T and $F_\beta = 78$ T. Temperature dependences of amplitudes of F_α and F_β are shown in the inset of (d). Dash lines are the fitting curves.

The coexistence of both high n and μ in a BaO film is a rare case. Therefore, we further explore the intrinsic states of BaO/STO under the magnetic fields. Principally, high RRR values and μ have enabled observations of quantum oscillations in electrical resistance. Firstly, we measured the Hall resistance (R_{xy}) [Fig. 3(a)] and MR $[R_{xx}(B) - R_{xx}(0)]/R_{xx}(0)$ [Fig. 3(b)] at T = 0.3–20 K and B up to 18 T. The magnetic fields were applied perpendicular to the surface plane ($B//c$). The R_{xx} of BaO/STO shows typical Shubnikov–de Haas (SdH) oscillations when T below 3 K and B above 5 T and the maximum value of MR is 1300% at 0.3 K and 18 T. The quantum oscillations become significant by plotting their amplitude values (ΔR_{xx}) against B^{-1} after subtracting a polynomial background [Fig. 3(c)]. Figure 3(d) shows the Fourier transformation analysis of the ΔR_{xx}–B^{-1} curves measured at 0.3–2.7 K. Two main components of the oscillations with frequencies F_α = 51 T and F_β = 78 T are deducted. The amplitudes of these two components decay gradually to zero with increasing temperature to 2.7 K. We calculate the effective masses of two types of electrons using the Lifshitz–Kosevich (L-K) equation

$$R_T = A'\left(\tfrac{m^*}{m_0}\right)T \Big/ \sinh\left[A'\left(\tfrac{m^*}{m_0}\right)T\right],$$

where $A' = 2\pi^2 k_B m^*/e\hbar H_{eff}$ and $H_{eff} = 2/(H_1^{-1} + H_2^{-1})$, in which H_1 and H_2 are the lower and upper limits of the magnetic field range of oscillations, respectively. R_T, m_0, m^*, k_B and $\hbar$ are the amplitude of the Fourier transformation (FT), free electron mass, effective mass, Boltzmann constant, and reduced Planck constant, respectively. By fitting the temperature-dependent oscillation amplitude [inset in Fig. 3(d)], we can obtain the effective masses of the two types of electrons are $m^*_\alpha = (1.15 \pm 0.12)m_0$ and $m^*_\beta = (1.31 \pm 0.18)m_0$, respectively. These values are comparable to the effective masses of other STO-based 2DEGs.[21,40,46,47] Simultaneously, the Dingle temper-

ature (T_D) and the total scattering time (τ) are determined to be 1.31 K (0.94 K) and 1.17 ps (1.29 ps), respectively, for F_α (F_β). The long τ provides independent evidence to the high μ in the BaO/STO heterojunction. It is more important that our samples are extremely sensitive to air and moisture even stocked in a glove box for a long time. The sample's degradation can drastically enhance the electron scattering and weaken the oscillations. Only the fresh samples can be observed to appear 2DEG with high μ.

The first-principles calculations were conducted to get a better understanding on the 2DEG at the interface BaO/STO. We carefully optimize the interface structure by minimizing the formation energy (Fig. S3) and compare the local density of states (LDOS) for each layer (Fig. S4). With the increasing layer thickness, the line shape of the LDOS does not change until the thicknesses of BaO and STO layers beyond 3 and 5 u.c., respectively. Therefore, we construct a supercell by stacking 3.5-u.c.-thick BaO over 5.5-u.c.-thick STO [Fig. 4(a)]. The upper panel of Fig. 4(b) displays the corresponding density of states (DOS), demonstrating that the BaO/STO interface keeps the insulating state. To explore the oxygen vacancy effect on the 2DEG, we create one and two oxygen vacancies of the BaO layer near the surface in a 2×2 superlattice (Fig. S5). In doing so, metallicity emerges as evidenced by the DOS plot in the bottom panel of Fig. 4(b). The layer projected DOS shows that the states across the Fermi level mainly come from the interface (Fig. S6), and these electrons are composed of Ti-3d_{xy} orbitals [Fig. 4(c)]. This is also confirmed by the electronic structure in Fig. S7. With these calculations, we obtain a deep insight into the formation of 2DEG of the STO/BaO interface. The perfect interface is insulating without oxygen vacancies of BaO, and then becomes metallic after introducing 12.5% oxygen vacancies. These emergent carriers will transfer to the Ti-3d t_{2g} orbital because this orbital is the lowest one under the TiO_6 octahedron crystal field. Hence, the effect of oxygen vacancies resembles electron doping.

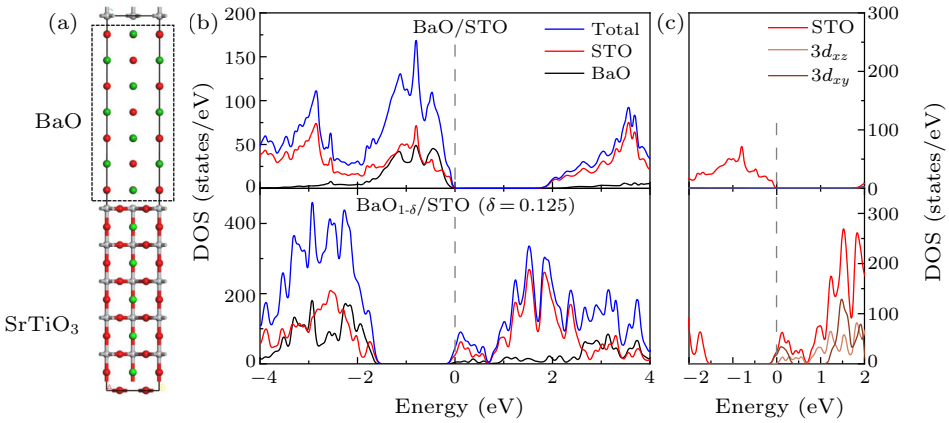

Fig. 4. Conducting interface between BaO and STO. (a) Schematic structure of proposed interface between 3.5 u.c. BaO and 5.5 u.c. STO. The green, grey and red balls are Ba/Sr, Ti, and O atoms, respectively. (b) Total and local density of states (DOS) of BaO/STO interface without (upper panel) and with (lower panel) oxygen vacancies in BaO layers. The oxygen vacancies are shown in Fig. S5. (c) The corresponding 3d orbitals of STO.

As for the origin of metallic behavior and such high mobility, a possible explanation is the existence of oxygen vacancy. Although the deposited $BaO_{1-\delta}$ could not absorb the same content of oxygen as Ba/STO does[48] under the same condition, it still can induce small amount of oxygen vacancies in both STO and $BaO_{1-\delta}$, favoring metallic conductivity. Compared with the reduced bulk-STO and most of STO-based heterojunctions, our sample exhibits a higher mobility. This may be due to the best lattice-matched and perfect interface between STO and $BaO_{1-\delta}$. Another scenario-like spatial separation between interfacial oxygen vacancies and the 2DEG is proposed in γ-Al_2O_3/STO, which can reduce the scattering from the defects and enhance electron mobility.[49] Further studies about the formation energy of oxygen vacancy in STO and BaO are needed. In addition, due to the water solubility of BaO,[24] a suitable protection to keep away from moisture is required.

In summary, we have shown the 2DEG formed at the oxides BaO/STO interface. We believe that the charge transfer at the interface, confirmed by our first-principles calculations, would be responsible for the observed quantum phenomena. Although the mechanism for the 2DEG with both high mobility and high concentration is not well understood, this work suggests that the rock-salt structure ionically compensated $BaO_{1-\delta}$ shows great potential for investigating the p–d electron correlation at the oxide interface and as a buffer or sacrifice layer to grow high-quality oxide-based compounds or superconductors.

Acknowledgments. We thank L. W. Guo, J. Y. Zhou and Y. L. Yang for helpful discussions. This work was financially supported

by the MoST-Strategic International Cooperation in Science, Technology and Innovation Key Program (Grant No. 2018YFE0202600), the National Key Research and Development Program of China (Grant Nos. 2017YFA0304700 and 2020YFA0309100), the National Natural Science Foundation of China (Grant Nos. 51922105, 51532010, and 11974390), the Beijing Natural Science Foundation (Grant Nos. Z200005, Z190010, and 2202060), the Strategic Priority Research Program of Chinese Academy of Sciences (Grant No. XDB33030200), and the Beijing Nova Program of Science and Technology (Grant No. Z191100001119112).

References

[1] Ohtomo A and Hwang H Y 2004 *Nature* **427** 423
[2] Herranz G, Basletic M, Bibes M, Ranchal R, Hamzic A, Tafra E, Bouzehouane K, Jacquet E, Contour J P, Barthélémy A and Fert A 2006 *Phys. Rev. B* **73** 064403
[3] Kalisky B, Bert J A, Klopfer B B, Bell C, Sato H K, Hosoda M, Hikita Y, Hwang H Y and Moler K A 2012 *Nat. Commun.* **3** 922
[4] Feng Y Q, Jin K J, Ge C, He X, Gu L, Yang Z Z, Guo H Z, Wan Q, He M, Lu H B and Yang G Z 2016 *Chin. Phys. Lett.* **33** 076801
[5] Dijkkamp D, Venkatesan T, Wu X D, Shaheen S A, Jisrawi N, Minlee Y H, McLean W L and Croft M 1987 *Appl. Phys. Lett.* **51** 619
[6] Bert J A, Kalisky B, Bell C, Kim M, Hikita Y, Hwang H Y and Moler K A 2011 *Nat. Phys.* **7** 767
[7] Ma Y, Niu J, Xing W, Yao Y, Cai R, Sun J, Xie X C, Lin X and Han W 2020 *Chin. Phys. Lett.* **37** 117401
[8] Liu C, Yan X, Jin D, Ma Y, Hsiao H W, Lin Y, Bretz-Sullivan T M, Zhou X, Pearson J, Fisher B, Jiang J S, Han W, Zuo J M, Wen J, Fong D D, Sun J, Zhou H and Bhattacharya A 2021 *Science* **371** 716
[9] Gao Q, Zhao Y, Zhou X J and Zhu Z 2021 *Chin. Phys. Lett.* **38** 077401
[10] Anh L D, Kaneta S, Tokunaga M, Seki M, Tabata H, Tanaka M and Ohya S 2020 *Adv. Mater.* **32** 1906003
[11] Lu D, Baek D J, Hong S S, Kourkoutis L F, Hikita Y and Hwang H Y 2016 *Nat. Mater.* **15** 1255
[12] Cantoni C, Gazquez J, Granozio F M, Oxley M P, Varela M, Lupini A R, Pennycook S J, Aruta C, di Uccio U S, Perna P and Maccariello D 2012 *Adv. Mater.* **24** 3952
[13] Bark C W, Sharma P, Wang Y, Baek S H, Lee S, Ryu S, Folkman C M, Paudel T R, Kumar A, Kalinin S V, Sokolov A, Tsymbal E Y, Rzchowski M S, Gruverman A and Eom C B 2012 *Nano Lett.* **12** 1765
[14] Huang Z, Han K, Zeng S, Motapothula M, Borisevich A Y, Ghosh S, Lu W, Li C, Zhou W, Liu Z, Coey M, Venkatesan T and Ariando 2016 *Nano Lett.* **16** 2307
[15] Zhang D, Lou W, Miao M, Zhang S C and Chang K 2013 *Phys. Rev. Lett.* **111** 156402
[16] Kalabukhov A, Gunnarsson R, Börjesson J, Olsson E, Claeson T and Winkler D 2007 *Phys. Rev. B* **75** 121404
[17] Herranz G, Basletic M, Bibes M, Carretero C, Tafra E, Jacquet E, Bouzehouane K, Deranlot C, Hamzic A, Broto J M, Barthelemy A and Fert A 2007 *Phys. Rev. Lett.* **98** 216803
[18] Caviglia A D, Gariglio S, Cancellieri C, Sacepe B, Fete A, Reyren N, Gabay M, Morpurgo A F and Triscone J M 2010 *Phys. Rev. Lett.* **105** 236802
[19] Breckenfeld E, Bronn N, Karthik J, Damodaran A R, Lee S, Mason N and Martin L W 2013 *Phys. Rev. Lett.* **110** 196804
[20] Nakagawa N, Hwang H Y and Muller D A 2006 *Nat. Mater.* **5** 204
[21] Chen Y Z, Bovet N, Trier F, Christensen D V, Qu F M, Andersen N H, Kasama T, Zhang W, Giraud R, Dufouleur J, Jespersen T S, Sun J R, Smith A, Nygard J, Lu L, Buchner B, Shen B G, Linderoth S and Pryds N 2013 *Nat. Commun.* **4** 1371
[22] Antoro I D and Kawae T 2021 *ECS J. Solid State Sci. Technol.* **10** 083005
[23] Gagnidze T, Ma H, Cancellieri C, Bona G L and La M F 2019 *Sci. Technol. Adv. Mater.* **20** 456
[24] Takahashi R and Lippmaa M 2020 *ACS Appl. Mater. Interfaces* **12** 25042
[25] Sayle D C and Watson G W 2001 *J. Phys. Chem.* **105** 5506
[26] Ron A, Hevroni A, Maniv E, Mograbi M, Jin L, Jia C L, Urban K W, Markovich G and Dagan Y 2017 *Adv. Mater. Interfaces* **4** 1700688
[27] Wu M K, Ashburn J R, Torng C J, Hor P H, Meng R L, Gao L, Huang Z J, Wang Y Q and Chu C W 1987 *Phys. Rev. Lett.* **58** 908
[28] Zhao Z X, Chen L Q, Yang Q S, Huang Y H, Chen G H, Tang R M, Liu G R, Cui C G, Chen L, Wang L H, Guo S Q, Li S L and Bi J Q 1987 *Kexue Tongbao* **32** 661 (in Chinese)
[29] Cava R J, Batlogg B, Vandover R B, Murphy D W, Sunshine S, Siegrist T, Remeika J P, Rietman E A, Zahurak S and Espinosa G P 1987 *Phys. Rev. Lett.* **58** 1676
[30] Jorgensen J D, Veal B W, Paulikas A P, Nowicki L J, Crabtree G W, Claus H and Kwok W K 1990 *Phys. Rev. B* **41** 1863
[31] Wen J G, Traeholt C and Zandbergen H W 1993 *Physica C* **205** 354
[32] Kresse G and Furthmuller J 1996 *Comput. Mater. Sci.* **6** 15
[33] Perdew J P, Burke K and Ernzerhof M 1997 *Phys. Rev. Lett.* **78** 1396
[34] Kresse G and Joubert D 1999 *Phys. Rev. B* **59** 1758
[35] Monkhorst H J and Pack J D 1976 *Phys. Rev. B* **13** 5188
[36] Matula R A 1979 *J. Phys. Chem. Ref. Data* **8** 1147
[37] Wang Z C, Chen L, Li S S, Ying J S, Tang F, Gao G Y, Fang Y, Zhao W, Cortie D, Wang X and Zheng R K 2021 *npj Quantum Mater.* **6** 53
[38] Tufte O N and Chapman P W 1967 *Phys. Rev.* **155** 796
[39] Szot K, Speier W, Carius R, Zastrow U and Beyer W 2002 *Phys. Rev. Lett.* **88** 075508
[40] Jalan B, Stemmer S, Mack S and Allen S J 2010 *Phys. Rev. B* **82** 081103
[41] Chen Y Z, Trier F, Wijnands T *et al.* 2015 *Nat. Mater.* **14** 801
[42] Zhang J, Ji W J, Xu J, Geng X Y, Zhou J, Gu Z B, Yao S H and Zhang S T 2017 *Sci. Adv.* **3** e1701473
[43] Cao M, Xiong D B, Yang L, Li S, Xie Y, Guo Q, Li Z, Adams H, Gu J, Fan T, Zhang X and Zhang D 2019 *Adv. Funct. Mater.* **29** 1806792
[44] Lee K, Kim S W, Toda Y, Matsuishi S and Hosono H 2013 *Nature* **494** 336
[45] Zhang J, Ok J M, Pai Y Y, Lapano J, Skoropata E, Mazza A R, Li H, Huon A, Yoon S, Lawrie B, Brahlek M, Ward T Z, Eres G, Miao H and Lee H N 2021 *Phys. Rev. B* **104** L161404
[46] Rubi K, Gosteau J, Serra R, Han K, Zeng S, Huang Z, Warot-Fonrose B, Arras R, Snoeck E, A, Goiran M and Escoffier W 2020 *npj Quantum Mater.* **5** 9
[47] Kim M, Bell C, Kozuka Y, Kurita M, Hikita Y and Hwang H Y 2011 *Phys. Rev. Lett.* **107** 106801
[48] Hill D M, Meyer H M and Weaver J H 1989 *J. Appl. Phys.* **65** 4943
[49] Schuetz P, Christensen D V, Borisov V, Pfaff F, Scheiderer P, Dudy L, Zapf M, Gabel J, Chen Y Z, Pryds N, Rogalev V A, Strocov V N, Schlueter C, Lee T L, Jeschke H O, Valenti R, Sing M and Claessen R 2017 *Phys. Rev. B* **96** 161409

Supplementary Material: Two-Dimensional Electron Gas with High Mobility Forming at BaO/$SrTiO_3$ Interface

Cheng Cao (曹程),[1,3,#] Shengru Chen (陈盛如), [1,2,#] Jun Deng (邓俊),[1] Gang Li (李岗),[1,4] Qinghua Zhang (张庆华),[1] Lin Gu (谷林),[1] Tian-Ping Ying (应天平),[1,4] Er-Jia Guo (郭尔佳),[1,2,4,*] Jian-Gang Guo (郭建刚),[1,4,*] and Xiaolong Chen (陈小龙)[1,2,4,*]

[1]Beijing National Laboratory for Condensed Matter Physics, Institute of Physics, Chinese Academy of Sciences, Beijing 100190, China.
[2] School of Physical Sciences, University of Chinese Academy of Sciences, Beijing 101408, China.
[3]College of Materials Science and Opto-Electronic Technology, University of Chinese Academy of Sciences, Beijing 100049, China.
[4]Songshan Lake Materials Laboratory, Dongguan, Guangdong 523808, China

[*]Corresponding author. Email: ejguo@iphy.ac.cn (Er-Jia Guo). jgguo@iphy.ac.cn (Jian-Gang Guo). chenx29@iphy.ac.cn (Xiaolong Chen).
#These authors contributed equally.

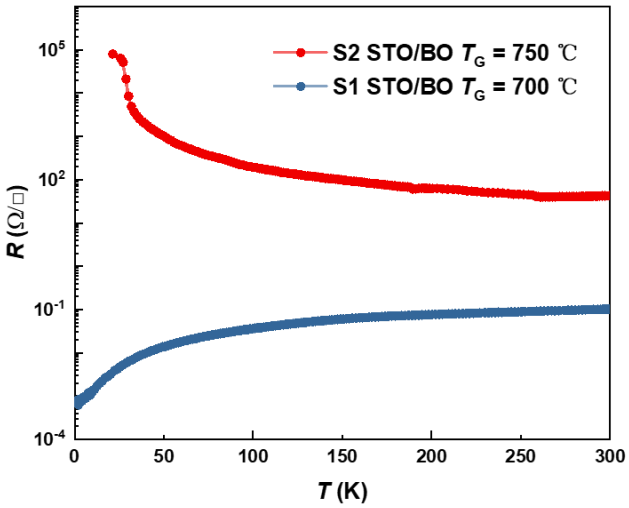

Figure S1. Temperature-dependent resistivity of BaO films under different growth temperatures. The BaO films grown at 700 ^{o}C (S1) exhibit a metallic behavior, whereas the BaO films grown at 750 ^{o}C (S2) is a semiconductor.

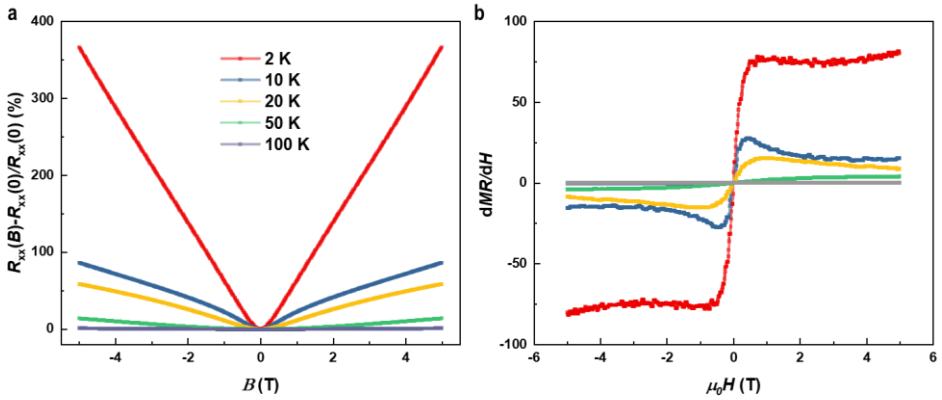

Figure S2. (a) Magnetoresistance [$R_{xx}(B)$-$R_{xx}(0)$]/$R_{xx}(0)$ and (b) the first derivative of MR, as a function of magnetic fields at various temperatures. We observe the linear MR beyond 0.5 T at 2 K.

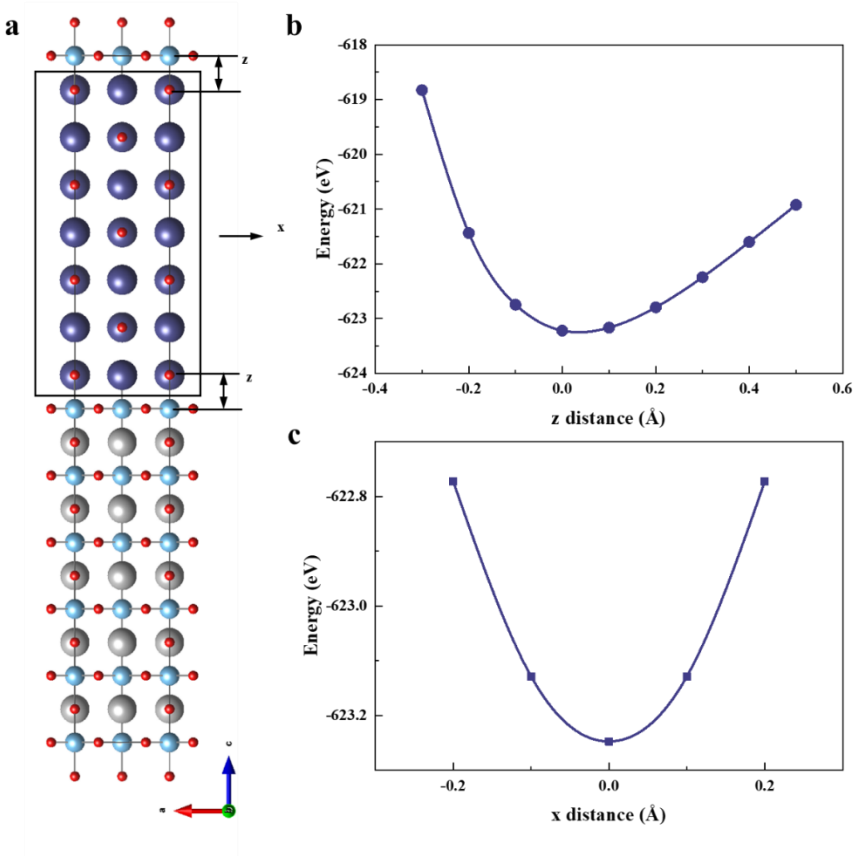

Figure S3. (a) Schematic of crystallographic structure of BaO/STO heterointerface. The optimized interface distance and stacking order are tested by moving BaO layers along (b) *z* and (c) *x* direction. And it is used as an initial model for further optimization.

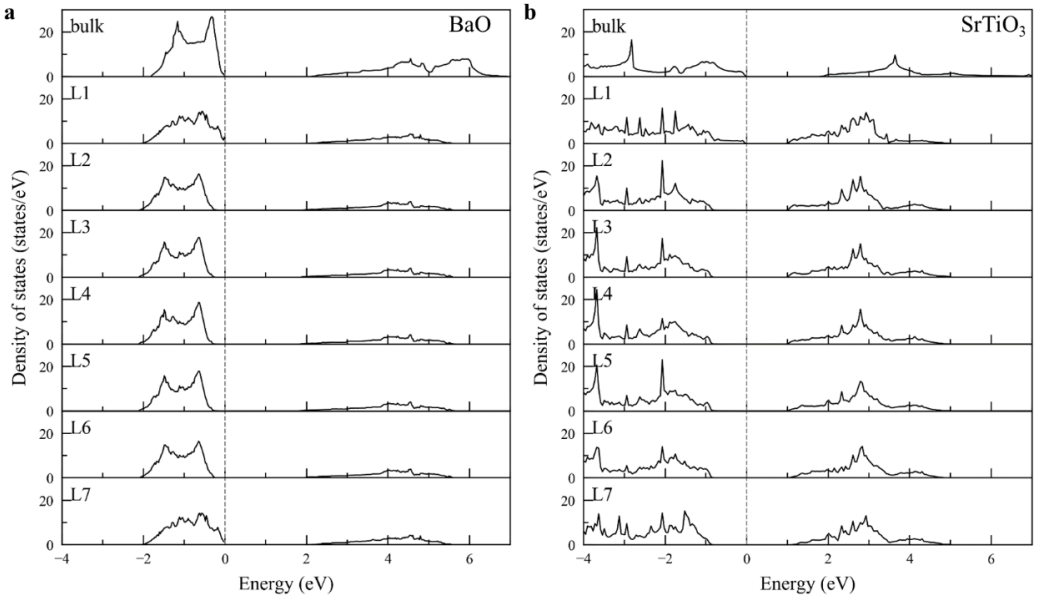

Figure S4. The local density of states of each layer for (a) BaO and (b) $SrTiO_3$. Firstly we build large slabs for BaO and $SrTiO_3$ and then calculate the local density of states (LDOS) for each layer to determine the thickness of STO/BaO that can keep the bulk properties. As the number of layers increasing, the line-shape of the LDOS does not change until the thickness of BaO and STO layers beyond 3 and 5 unit cells (u. c.), respectively. In this work, we choose 3.5-u.c.-thick BaO and 5.5-u.c.-thick STO to build the STO/BaO interface.

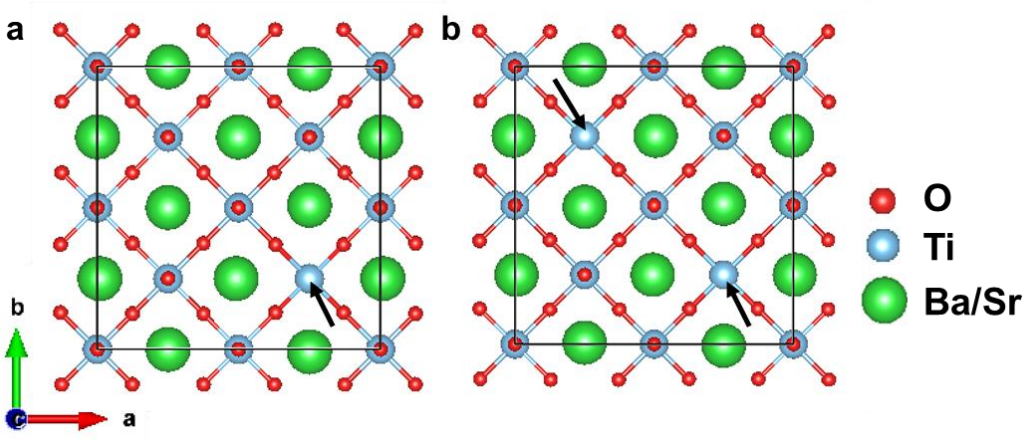

Figure S5. One (a) and two (b) oxygen vacancies of BaO layer near the surface in a 2×2 superlattice.

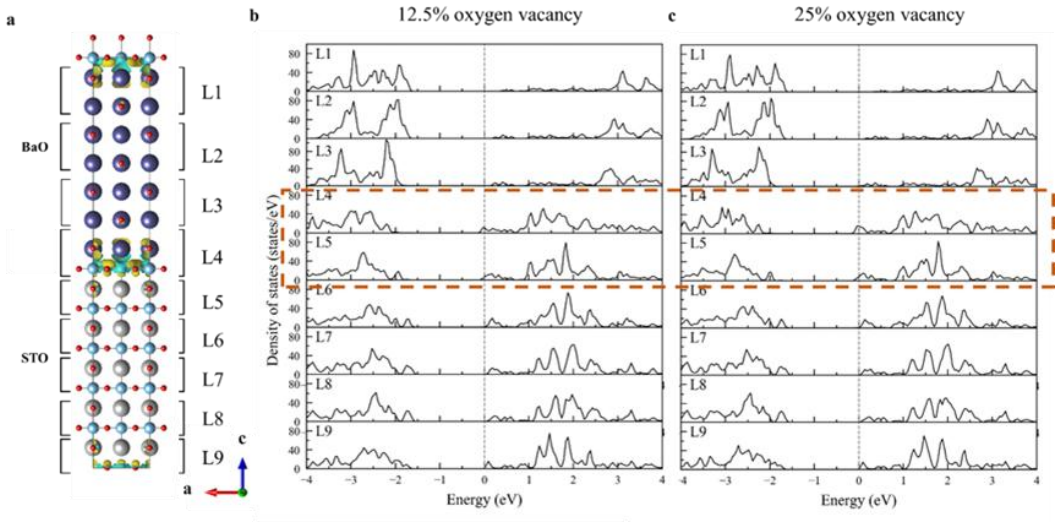

Figure S6. (a) Charge density difference at the BaO/STO heterointerfaces. (b) The local density of states (LDOS) for BaO layers containing 12.5% oxygen vacancies. (c) LDOS for each layer of BaO layers containing 25% oxygen vacancies.

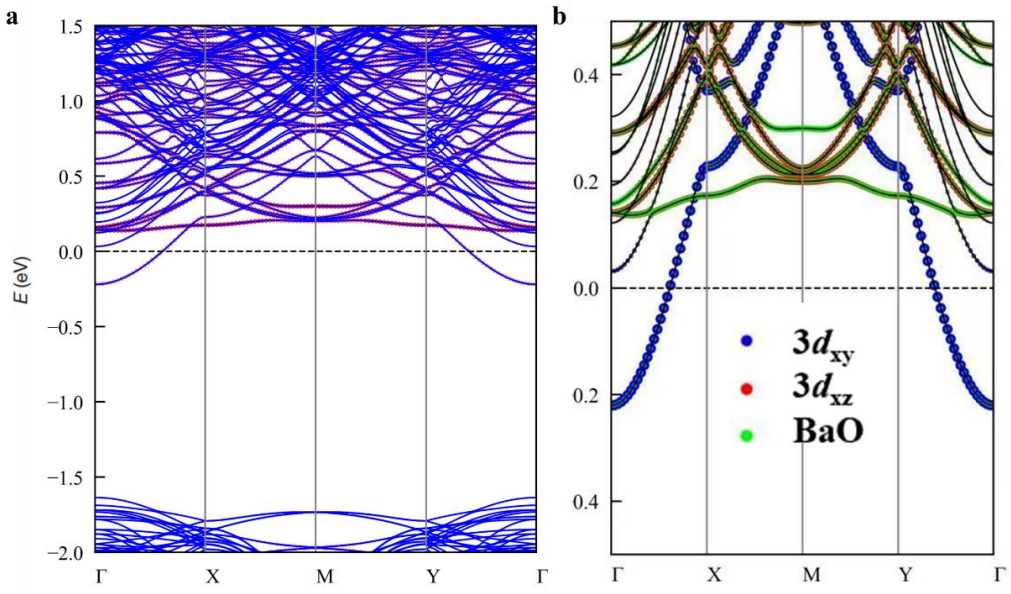

Figure S7. (a) Calculated electronic structure of $BaO/SrTiO_3$ heterointerfaces. Dashed line represents the Fermi level (E_F). (b) Enlarged plot of band structure around the E_F. The blue, red and green lines represent contributions of Ti-3d_{xy}, Ti-3d_{xz} orbitals and BaO orbitals, respectively.